Sensitivity of electrospray molecular dynamics simulations to long-range Coulomb interaction models

Neil A. Mehta and Deborah A. Levin
The University of Illinois Urbana-Champaign, Champaign, Illinois 61801, USA

(Received 27 September 2017; published 12 March 2018)

Molecular dynamics (MD) electrospray simulations of 1-ethyl-3-methylimidazolium tetrafluoroborate (EMIM-BF_4) ion liquid were performed with the goal of evaluating the influence of long-range Coulomb models on ion emission characteristics. The direct Coulomb (DC), shifted force Coulomb sum (SFCS), and particle-particle particle-mesh (PPPM) long-range Coulomb models were considered in this work. The DC method with a sufficiently large cutoff radius was found to be the most accurate approach for modeling electrosprays, but, it is computationally expensive. The Coulomb potential energy modeled by the DC method in combination with the radial electric fields were found to be necessary to generate the Taylor cone. The differences observed between the SFCS and the DC in terms of predicting the total ion emission suggest that the former should not be used in MD electrospray simulations. Furthermore, the common assumption of domain periodicity was observed to be detrimental to the accuracy of the capillary-based electrospray simulations.

DOI: 10.1103/PhysRevE.97.033306

I. INTRODUCTION

Ionic liquids (ILs) are a class of salts, with melting point typically lower than 373 K, that have good electrical conductivity, thermal stability, and low vapor pressure. The combination of these unique properties allows ILs to atomize in the presence of an external electric field into a jet of ions or droplets. This formation of jets or electrosprays by ionic liquids in the presence of electric field occurs through the formation of a Taylor cone [1]. After emission, the ions or droplets emitted by the Taylor cone are further accelerated due to the external electric field, generating thrust. Electrosprays are an important tool in microfabrication because they can be used to control deposition [2] in applications involving microfilm deposition [3], microcircuit manufacturing [4], and ion beam lithography. [5] The electrosprays of charged liquids also find applications in the fields such as biomedical engineering [6,7], especially in the analysis of biological tissues [8], microelectromechanical systems (MEMS), pharmaceutical development [9,10], food sciences [11], and other industrial [12,13] engineering applications. Electrosprays are also used to analyze the properties of ILs using electrospray ionization mass spectroscopy (ESI-MS) [14]. For aerospace micropropulsion applications, the ability to generate accelerated jets also makes ionic liquids useful as propellants in colloid thrusters [15,16]. These colloid thrusters, also known as microthrust devices, are useful for orbit correction and station keeping of small satellites. Regardless of the application, however, the physics of Taylor cone formation [1] is still not completely understood.

The ability to predict the electrochemical behavior of ILs using molecular dynamics (MD) and the availability of MD interatomic potentials such as OPLS [17], can lead to a better understanding of many different ILs used in electrosprays. For example, previous work by Kim *et al.* [18] and Borner *et al.* [19], have demonstrated the capability of MD to successfully simulate liquid gallium and 1-ethyl-3-methylimidazolium tetrafluoroborate (EMIM-BF_4) electrosprays using MD to obtain the thrust and emission current from the predicted ionic byproducts. However, all electrospray MD simulations are strongly influenced by the selection of the long-range interaction models. Work by Weingartner [20], suggests that in simple salts, the long-range Coulomb interactions control the intermolecular interactions. Lee *et al.* [21] state that long-range Coulomb interactions have a significant effect on the fluid properties of the ILs predicted by quantum-mechanical-based models. Brooks *et al.* [22] have additionally shown structural effects that arise in ionic liquid simulations due to approximate treatment of electrostatic interactions from periodic boundary conditions. They also state that an incorrect termination of the long-range Coulomb interactions destroys the structural effects such as charge layering in their charged argon-based simulation. The short-range Coulomb interactions over a radius of 10–15 Å are adequate in charge dense systems that are periodic. However, electrospray simulation domains have regions where the emitted ions are farther apart, leading to low charge density farther away from the capillary. This makes it vital to use the correct long-range Coulomb interaction model when simulating ionic liquids with charge sparse regions.

The objective of this work is to quantify the sensitivity of electrospray emission modes to the method of calculation of long-range Coulomb forces. The variation of long-range Coulomb contributions to the selection of cutoff radii and its change on the outcome of the MD electrospray simulations was explored. MD simulations typically scale as $O(N^2)$, where N is the number of atoms used for the simulation. Thus, it is not viable to use an infinite cutoff radius, as the solutions become prohibitively expensive. Also, the Coulomb forces and energies at the cutoff radius that separates the long-ranged and short-ranged forces must be matched. We, therefore, face a twofold problem of performing simulations with converged cutoff radius for the short-range Coulomb interactions as well as having an accurate long-range model appropriate for the electrospray simulations.

In this work, we investigate the effects of long-range Coulomb models on the electrospray emissions using the coarse-grained (CG) EMIM-BF_4 potential of our previous work [19]. In Sec. II, we provide the details of the MD simulation geometry and the electrical boundary conditions used to implement the applied electric field responsible for extrusion of the IL from a capillary and the typical long-range Coulomb interaction models used for MD simulations are briefly discussed in Sec. III. The effects of these long-range Coulomb interaction models on the Taylor cone formation and the emission of ions sampled from the electrospray simulations are discussed in Sec. IV A. Similarly, the ion emission currents of different ion species and the Coulomb energy of the system are used to analyze the dependence of Coulomb cutoff radius on electrospray simulations in Sec. IV B. Finally, the effect of periodic boundary conditions on Coulomb potential energy and its subsequent effects on ion emissions are discussed in Sec. IV C.

II. NUMERICAL PARAMETERS AND POTENTIALS USED FOR THE MD SIMULATIONS

All MD simulations for this work were performed using the LAMMPS [23] MD package. The all-atom model of EMIM-BF_4 and its corresponding coarse-grained (CG) model are shown in Figs. 1(a) and 1(b), respectively. The CG potential allows the simulation to be performed using just five CG sites instead of 27 atoms required for an all-atom simulation by simplifying groups of nonessential degrees of freedom into a single site [24]. The coarse-grained potential for the EMIM-BF_4 was obtained by modifying the CG EMIM-NO_3 potential derived by Wang *et al.* [24,25] using the effective field coarse graining method (EFCG). This method allows large molecular groups within an ion pair to be treated as a single CG site. The positions the CG groups were calculated from the center of mass of all the constituent atoms forming those CG groups. The masses and charges of the CG sites were simply the sum of the masses and partial charges of the atoms forming the CG sites. The all-atom EMIM-BF_4 ion pair, shown in Fig. 1(a) was simplified to CG EMIM-BF_4, shown in Fig. 1(b), by approximating the cation complex imidazolium, methylene, and two methyl groups to CG groups IM, MR, M1, and M2, respectively. Similarly, the anion BF_4^- was also approximated as a single CG site. The EFCG method uses separate treatments to calculate the bonded and nonbonded interactions. The bonded interactions, namely, the covalent bonds, angles, and dihedrals were simulated using a harmonic function. The nonbonded interactions were modeled during the simulations using the tabulated potentials calculated from EFCG, for a combination of each CG site. The bonded and nonbonded CG potentials used for this work have been provided as Supplemental Material [26]. The extrusion simulations were performed using 256 cores of Intel Xeon Phi 7250 (Knights Landing) nodes on the STAMPEDE 2 machine, employing the parallelized version of the PPPM and DC methods and required approximately 38 h each to complete a simulation time of 1.0 ns. The PPPM model was used with the desired relative error in forces with accuracy of 1×10^{-5} for all our simulations.

To understand the effects of long-range Coulomb interactions and the electric field boundary conditions, relatively

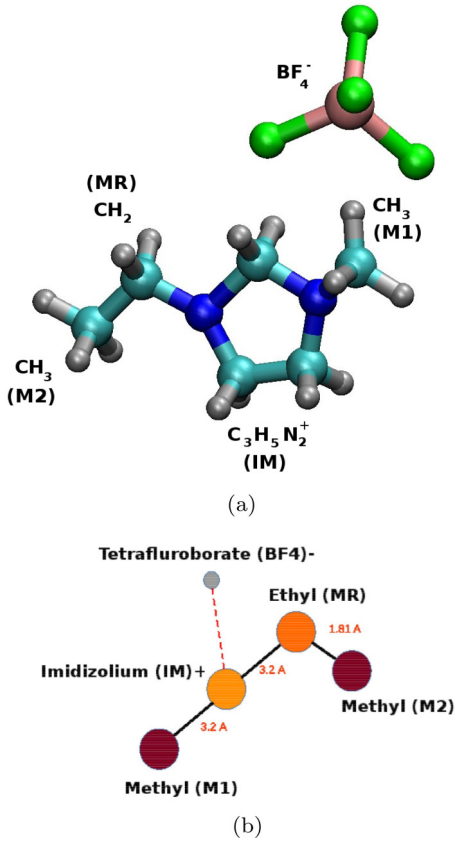

FIG. 1. All-atom (a) and corresponding coarse-grained model (b) of EMIM-BF_4. For the all-atom model, atom colors are as follows: C (teal, larger light gray), H (silver, smaller light gray), N (blue, dark gray), B (pink, larger), and F (green, smaller). Each EMIM-BF_4 is approximately 6 Å across in dimension.

larger scale (>10 000 atoms) MD simulation domain, as shown in Fig. 2(a), was designed. A capillary of radius 56 Å and length 275 Å was constructed using 16,626 platinum atoms. The capillary was filled with 9455 molecules of EMIM-BF_4 which were first energy minimized and then thermally equilibrated to room temperature. The desired flow within the capillary was generated using a repulsive moving wall with a Lennard-Jones 9-3 potential. The capillary was placed within a domain of size 500 × 500 × 1,375 Å, at the $z_{\min} = 0$ Å of the domain. An extractor ring was placed at $z = 1275$ Å, positioning it 1000 Å away from the mouth of the capillary. A negative potential was applied at the extractor and the ground potential was applied at the mouth of the capillary. An external electric field was obtained for these simulations by solving the Laplace's equation for the appropriate boundary conditions, as will be discussed in Sec. III. The species-specific extraction current was obtained by sampling the emitted ion pairs at the extractor plane. It should be noted that with the exception of the direct Coulomb method, the other long-range Coulomb interaction methods require the domain to be periodic in all three dimensions. However, it is not possible to have the domain periodic in the extrusion direction, i.e., along the z axis. Therefore, a combination of *evaporate* and *slab* procedures were used along the x-y plane at $z_{\max}$ of the domain in LAMMPS to generate a quasiperiodicity in the extrusion direction for simulations

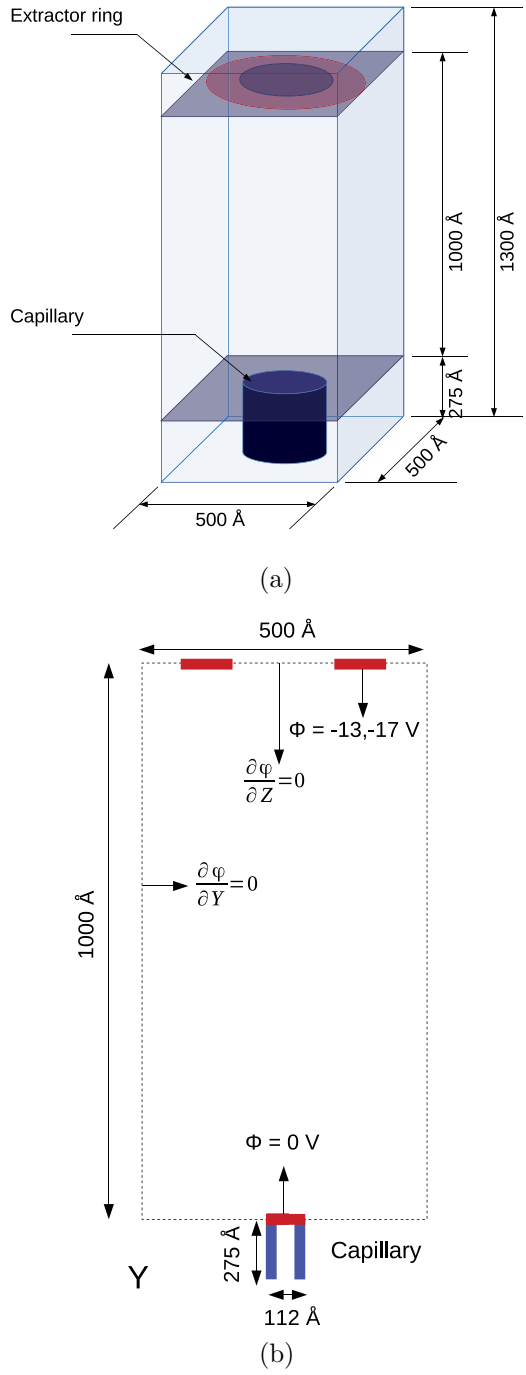

FIG. 2. Schematic of an MD electrospray simulations (a) and boundary conditions used for extrusion simulations (b).

that explicitly required periodicity in all three dimensions. The evaporation procedure allows one to remove atoms from a specified region, which in our case is a rectangular box of size $500 \times 500 \times 20\,\text{Å}^3$ placed right beyond the extractor plane. Removing atoms beyond the extractor ensures that particles leaving the domain at $z_{\max} = 1375$ Å do not reenter from $z_{\min}$ due to periodicity. To shield the electrostatic contributions of these outbound ion pairs on the atoms near $z_{\min}$, the slab fix inserts an empty volume between the periodic images. This effectively allows the boundary to be treated as quasiperiodic, turning off the long-range Coulomb interactions along that periodic boundary.

III. LONG-RANGE COULOMB INTERACTION MODELS

The electrostatic energy, E_{Coul}, for a system of charged particles is calculated using Coulomb's relationship,

$$E_{\text{Coul}} = \sum_{i=1}^{n-1} \sum_{j=i+1}^{n} C \frac{q_i q_j}{r_{ij}}, \tag{1}$$

where n is the total number of atoms in the system, r_{ij} is the distance between atoms i and j, C is known as the Coulomb constant, and q_i,q_j are the user-defined partial charges on atoms i and j, respectively, and are typically obtained from density functional theory (DFT) calculations that are used to define the interaction potential. The values of q_i can be found in Table 2.1 of Ref. [19]. The electrostatic interaction energy, observed from Eq. (1), scales as $1/r$ and even a small change in the interatomic distance leads to a large fluctuation at short distances. For simulations having large spatial dimensions or with large number of atoms (>10 000), the electrostatic energy calculations using Eq. (1) can be computationally expensive. The spatial distances become especially large when periodic boundary conditions are used, since the simulation box now becomes infinite in length. To overcome this limitation, the electrostatic energy calculations are split into short- and long-range Coulomb interactions, where the latter is the electrostatic energy calculated at long ranges beyond the user selected short-range cutoff distance R_c. From the computational point of view, the electrostatic energy is now calculated as

$$E_{\text{Coul}} = E_{\text{short-range}} + E_{\text{long-range}}, \tag{2}$$

where the first and second terms are associated with the designations of E_{direct} and E_{mesh}, respectively [27], and

$$E_{\text{short-range}} = E_{\text{direct}} = \sum_{i=1}^{n-1} \sum_{j=i+1}^{n} C \frac{q_i q_j}{r_{ij}},\ r_{ij} < R_c. \tag{3}$$

The purpose of this splitting of the Coulomb energies is to use a comparatively computationally inexpensive Coulomb interaction approximation at distances larger than the cutoff radius while ensuring that the short-range interactions are calculated directly using Eq. (1). Using Eq. (1) for short-range interactions provides the best accuracy for the interactions between closest particles which generates the largest contribution to the sum of all pairwise interactions. Of course, in an ideal case we would calculate all the Coulombic interactions using Eq. (1) assuming an infinitely large cutoff radius. We will evaluate some extrusion conditions in this work for a cutoff radius much larger than is typically used to understand the effect on the MD simulations and will refer to these simulations as using the direct Coulomb (DC) approach.

There are a number of methods available for the calculation of the long-range or E_{mesh} part of the electrostatic interaction which vary in their complexity from the simple shifted force Coulomb sum (SFCS) to the complex Ewald's sum method. The SFCS method [28] works on the principles of truncating and dampening the Coulombic interaction over large distances. SFCS is, computationally, the least expensive of the long-range

models but due to the truncation and dampening of Coulombic interactions beyond the cutoff radius R_c, this method is used primarily for preparation of systems for further simulations using models with better accuracy. More complex methods like Ewald's summation use Fourier transformations to compute the long-range interactions. These methods are computationally more expensive than the SFCS method but provide good accuracy. Finally, the particle-particle particle-mesh (PPPM) [29] is one variant of the Ewald's summation method and is attractive for systems with large numbers of atoms because it scales as $N\log_2(N)$ instead of a double summation N^2 scaling. The mathematics and implementation details of the PPPM method are provided in work by Pollock and Glosli [30], Darden *et al.* [31], and Toukmaji and Board Jr. [32]. We briefly discuss the methodology of using it to evaluate the E_{mesh} term below.

The E_{mesh} term is calculated by mapping the charged particles to the mesh nodes of a grid superimposed on the MD simulations to solve for the potential using the Poisson equation,

$$\nabla^2\phi_p(\bar{R}) = -\frac{1}{\epsilon}\rho(\bar{R}), \tag{4}$$

where ϵ is the vacuum permittivity and $\rho(\bar{R})$ and $\phi_p(\bar{R})$ are the charge density and electrostatic potential obtained by solving Poisson's equation at the grid nodes with position vector $\bar{R}$. The charge density is defined as the total charge present per grid cell volume,

$$\rho(\bar{R}) = \frac{q(\bar{R})}{h_x h_y h_z}, \tag{5}$$

where h_x, h_y, h_z are the fixed, constant grid cell sizes in x, y, and z, respectively. The charges $q(\bar{R})$ are obtained using a mapping scheme such that the charges present in the grid cell are distributed to the eight nodes of the cell using particle weighting. The charge on a grid point is calculated as

$$q(\bar{R}) = \sum_{i=1}^{8} q_i \bar{W}(\bar{r}_i - \bar{R}), \tag{6}$$

$$\bar{W} = W_x W_y W_z, \tag{7}$$

$$W_x(r_{i,x} - R_x) = 1 - \begin{cases} \frac{\delta}{h_x} & \text{for } \delta < h_x \\ 0 & \text{for } \delta \geqslant h_x \end{cases}, \tag{8}$$

$$\delta = |r_{i,x} - R_x|, \tag{9}$$

where $\bar{W}$ is the weight assigned to the interaction depending on the distance between the position vector of the ith particle $\bar{r}_i$ and the grid node position vector $\bar{R}$.

Typically, it is computationally feasible to calculate the short-range Coulombic interactions using Eq. (1) for R_c less than 12 Å. This makes it necessary to calculate the long-range Coulomb interaction using E_{mesh} for grid sizes h_x, h_y, and h_z, equal to 12 Å. Since a molecule of EMIM-BF_4 spans approximately 10 Å across, the E_{mesh} grid size of $h_x = h_y = h_z$=12 Å should be optimum for our MD EMIM-BF_4 simulations. The field generated by the potential obtained at each grid node from the solution to the Poisson's equation is given as

$$\bar{E}_k = -\bar{\nabla}\phi_p(\bar{R}), \tag{10}$$

where $\bar{E}_k$ is the field at the k^{th} grid node. The effective long-range Coulomb energy, $E_{\text{long-range}}$ or E_{mesh} on an atom due to the field generated in Eq. (10) is given as

$$E_{\text{mesh}} = E_{\text{long-range}} = \sum_{i=1}^{n} \int \bar{F}_{ki}\, d\bar{r}_{p_i}, \tag{11}$$

where

$$\bar{F}_{ki} = q_i \bar{E}_k, \tag{12}$$

such that $\bar{F}_{ki}$ is the force on the i^{th} atom due to the electric field contribution from the grid node k and $\bar{r}_{p_i}$ is the vector joining the position vector of the atom with the position vector of the grid node. With these definitions, the total Coulomb potential energy of the system is therefore the sum of the energies given in Eqs. (3) and (11).

The total electric potential felt by the ith atom may be written as

$$\varphi_{\text{tot}_i} = C q_i \sum_{\substack{i\neq j \\ r_{ij}<R_c}}^{n} \frac{q_j}{r_{ij}} + \varphi_p + \varphi_l, \tag{13}$$

where the first term is the short-ranged potential calculated by the direct Coulomb approach, with a cutoff radius R_c, the second term is obtained from the solution of Poisson's equation using the PPPM method, and the third term is due to an externally applied electric field, constant in time. In Eq. (13), the first two terms are analogous to "space charge" since they represent the effect of the induced electric field, but at the atomistic level. Once the electrical boundary conditions are specified, such as in Fig. 2(b), φ_l can be obtained from Laplace's equation,

$$\nabla^2\phi_l = 0, \tag{14}$$

using the generalized minimal residual (GMRES) method [33] with a grid size (h_x, h_y, and h_z) equal to the Coulomb cutoff radii R_c. A Neumann boundary condition was applied in the periodic x-y and nonperiodic z directions, except at the extractor ring and the capillary, as shown in Fig. 2(b). Note that this contribution to the total electric potential on an atom only needs to be computed once, at the zeroth time step, whereas the first and second terms of Eq. (13) are computed every time step in the MD simulation. Grid convergence for Eq. (14) was tested by reducing the grid size from 12 to 5 Å. As opposed to a constant normal electric field, the spatially varying electric field in the direction of extrusion defined by this configuration is strongest at the mouth or meniscus of the capillary and becomes gradually weaker farther away from the capillary. Also in contrast to a constant normal electric field with no radial component, the radial electric field enhances the formation of the Taylor cone.

IV. RESULTS AND DISCUSSIONS FROM THE MD EXTRUSION SIMULATIONS

A. Ion emission behavior for different long-range Coulomb interaction models

Two sets of MD simulations were performed using two different long-range Coulomb interaction methods. For the first, the Coulombic interactions were calculated solely using Eq. (3) for both short and long range, referred to as the DC method, with an extended cutoff radius of 20 Å. For the second set of simulations, the short-range Coulombic interactions were calculated using Eq. (3) with a cutoff radius of R_c = 12.0 Å and beyond R_c, the long range was calculated using the PPPM method, as described by Eqs. (4)–(12), with desired relative error in forces of 1.0×10^{-5}. The grid size used by the PPPM method was equal to the cutoff radius R_c = 12 Å. For both sets of simulations the mass flow rate was varied from 1.22×10^{-12}, 2.44×10^{-12}, 4.88×10^{-12}, 7.32×10^{-12}, and 9.76×10^{-12} kg/s. Emission results from these simulations were then compared with those obtained by Borner *et al.* [19,34,35] for their EMIM-BF_4 simulations using the SFCS long-range Coulomb model and the electrospray experiments performed by Romero-Sanz *et al.* [36].

An electrospray device operates either in a positive or negative mode of operation. If a negative potential is applied at the extractor, it acts as a cathode and the electrospray is said to operate in a positive mode of operation. For the MD simulations, a negative extraction potential of −13 V was applied and so positive ion species were sampled at the extractor. The emitted positive ion species were classified based on the number of cations present in the aggregate. Using the definition, $(\mathrm{EMIM} - \mathrm{BF_4})_n \times \mathrm{EMIM}^+$, if n was zero, the aggregate was termed a *monomer* and if n = 1 or 2, the aggregate was defined as a *dimer* or *trimer*, respectively. For n larger than 9, the aggregates were defined as a droplet. The emitted ions were sampled at the annular extractor ring, 1000 Å away from the capillary and the emission currents were calculated as a cumulative time moving average for the sampled ion species obtained at every 10 ps. The emission currents shown in this work were averaged for approximately 750 ps. The approximate number of monomers, dimers, trimers, and droplets emitted at lowest mass flow rate of 1.22×10^{-12} kg/s was found to be 62, 49, 80, and 10, respectively.

A comparison of the emitted monomer currents for the entire mass flow rate range is shown in Fig. 3(a). We observed that while the coupled DC + PPPM and SFCS methods overpredicted the monomer emission currents, the DC method produced good agreement with the experiments for all mass flow rates. However, this agreement did not extend to the dimer, trimer, and droplet current for any of the three MD Coulomb interaction methods, as shown in Figs. 3(b), 4(a), and 4(b), respectively. The MD results from the DC and coupled DC + PPPM method underpredicted the dimer current compared to the experiments. Use of the SFCS model, however, leads to a weaker system Coulombic energy resulting in even higher emission rates of larger emission species and hence the overprediction of the dimer current. All three MD methods overpredicted the trimer and droplet currents compared to the experiments. While, the extraction potential of −13 V was adequate in generating strong enough normal and radial

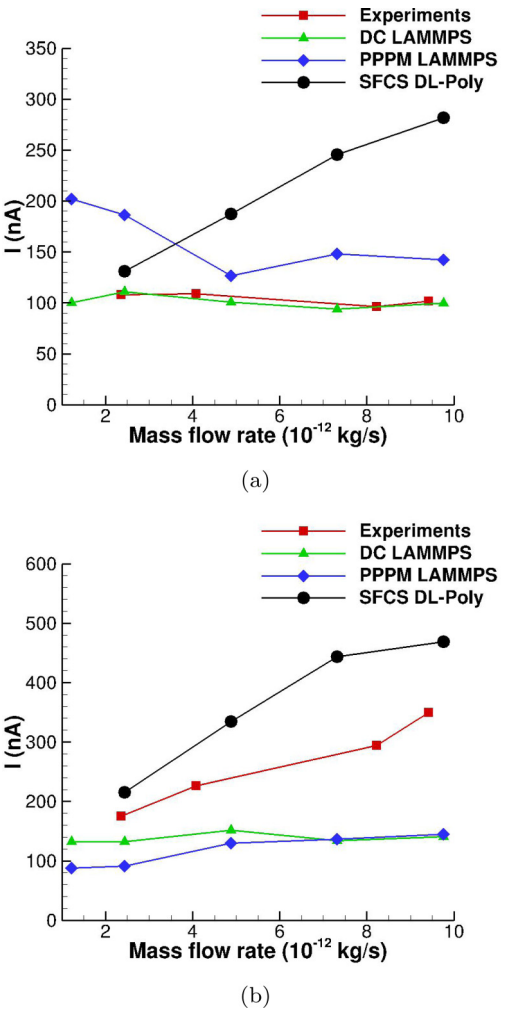

FIG. 3. Emission current of monomer (a) and dimer (b) species sampled at the extraction plane, shown as a cumulative moving average at every 5 ps for mass flow rates of 1.22×10^{-12}, 2.44×10^{-12}, 4.88×10^{-12}, 7.32×10^{-12}, and 9.76×10^{-12} kg/s.

electric fields near the mouth of the capillary, it did not produce sufficiently strong normal electric fields farther away from the capillary to break the larger aggregates into smaller species. This causes the MD simulations to predict higher trimer as well as droplet currents. The agreement of the total ion current (sum of monomer, dimer, and trimer), shown in Fig. 5(a), from the DC and coupled DC + PPPM method with the experiment was achieved because the overprediction of trimer and droplet currents compensated the underpredicted dimer currents. The SFCS method showed large disagreement with the experiment on account of weaker Coulombic interactions, especially at higher mass flow rates for all ion species except trimers. The larger emitted ion species underwent subsequent breakdown into smaller ion species due to the weaker Coulomb interactions. The large droplet currents from all MD methods caused the total emission current to be higher than the experiment values, as shown in Fig. 5(b), but despite that, the DC and coupled DC + PPPM methods compared better than the SFCS method for the total emission currents. Given the approximations inherent in the SFCS method and its level of accuracy, it should therefore be avoided when performing

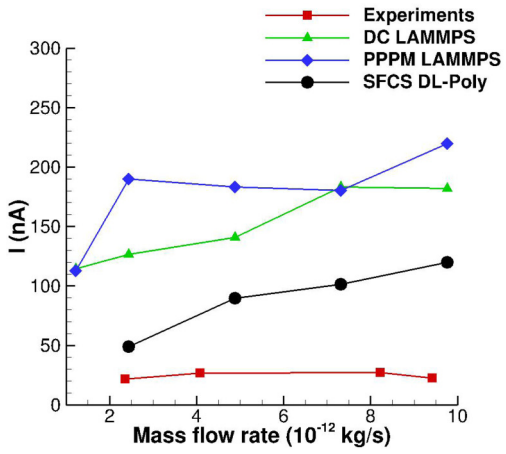

(a)

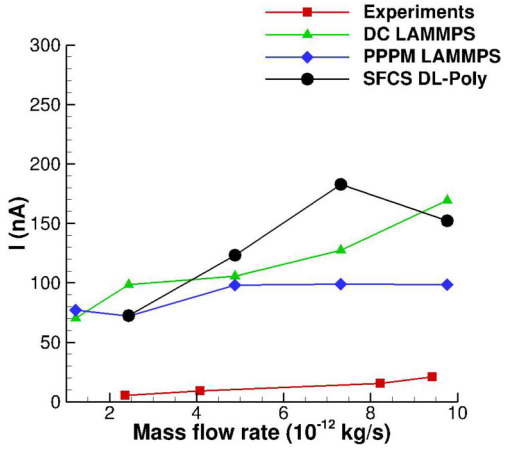

(b)

FIG. 4. Emission current of trimer (a) and droplets (b) sampled at the extraction plane, shown as a cumulative moving average at every 5 ps for mass flow rates of 1.22×10^{-12}, 2.44×10^{-12}, 4.88×10^{-12}, 7.32×10^{-12}, and 9.76×10^{-12} kg/s.

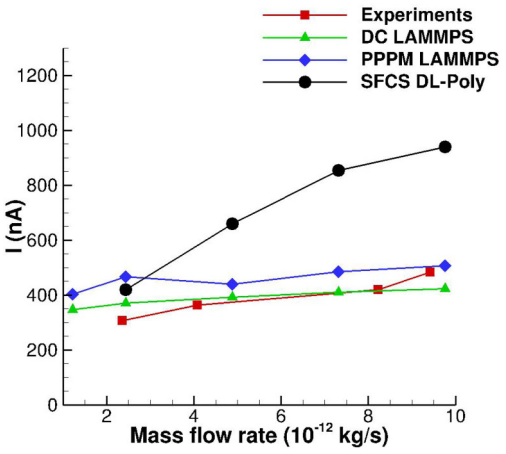

(a)

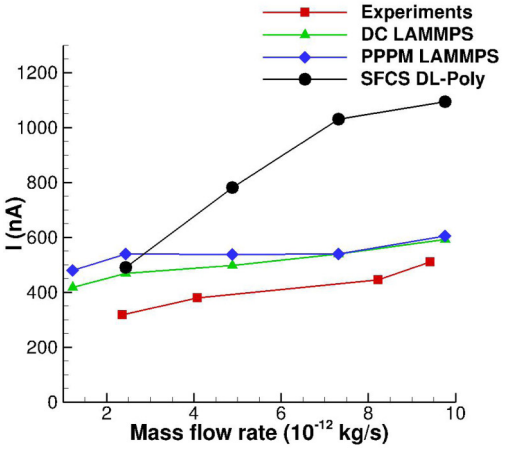

(b)

FIG. 5. Ion (sum of monomer, dimer, and trimer) (a) and total (b) emission current sampled at the extraction plane, shown as a cumulative moving average at every 5 ps for mass flow rates of 1.22×10^{-12}, 2.44×10^{-12}, 4.88×10^{-12}, 7.32×10^{-12}, and 9.76×10^{-12} kg/s.

electrospray MD simulations due to its failure to generate sufficiently strong Coulomb interactions.

The difference in the evolution of the Taylor cone structure and the emission behavior can be deduced from the rate of ion emissions and the Coulombic energy per emitted ion. For this comparison, we analyzed the electrospray simulation at the lowest mass flow rate of 1.22×10^{-12} kg/s. As observed from Fig. 6(a), the ion emission characteristics for the DC and the coupled DC + PPPM were fundamentally different. The emission of ions predicted by the coupled DC + PPPM was initially and continually larger, whereas the DC method showed gradual emission at a much lower rate. The snapshots of ion emission for the DC and coupled DC + PPPM method at approximately 400-ps simulation time are also shown in Figs. 7(a) and 7(b), respectively. The gradual increase in the ion emission for the DC method leads to a distinct cone structure formation at the mouth of the capillary after which emission occurs at the apex of the cone-shaped structure. As previously mentioned, the presence of the radial electric field also helps the formation of the cone structure. This is reflected from the gradual increase in the emission of ion pairs up to 350 ps and then higher emission beyond 350 ps in Fig. 6(a).

A comparison of Coulomb energy per ion of emitted ions is shown in Fig. 6(b). In the DC method, the build-up of the Taylor cone and emission of only monomers up to 350 ps leads to a positive Coulomb energy per ion for the emitted ions. Beyond 350 ps, once the Taylor cone was fully formed, larger ion species were emitted from the apex. For the coupled DC + PPPM method, emission was observed to contain monomers and larger species from the start of the simulation. The sparse distribution of the emitted species and the presence of anions in the larger ion species lead to negative Coulomb energy per emitted ion for the coupled DC + PPPM method throughout the duration of the simulation and for the DC method beyond 350 ps. For the DC + PPPM method, after 400 ps, a large number of ion pairs were spontaneously emitted in the domain, lowering (less negative) the Coulomb energy per emitted ion.

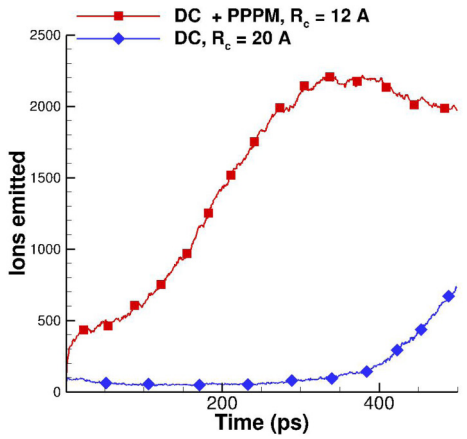

(a)

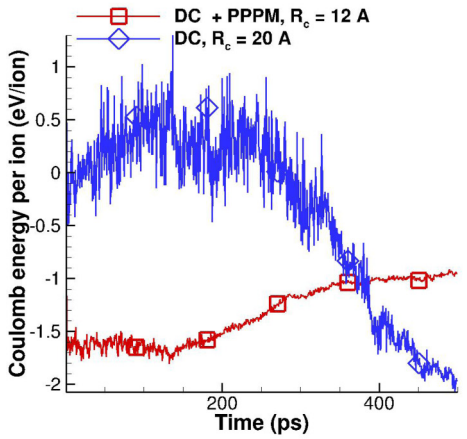

(b)

FIG. 6. Comparison of number of ions emitted (a) and Coulomb energy per ion of emitted ions (b) for the DC and DC + PPPM coupled Coulomb interactions, for an EMIM-BF_4 electrospray simulation at a mass flow rate of 1.22×10^{-12} kg/s and extraction potential of -13 V.

B. Effect of Coulomb cutoff radius, R_c, and E_{mesh} grid size on emission

It was found from MD simulations that the effects of cutoff radius were most evident at lower mass flow rates and for a high extractor ring potential. Therefore, the simulations discussed in this section were performed for a mass flow rate of 1.22×10^{-12} kg/s and an applied extractor potential of -17 V. We consider the DC method with a large R_c to be the most accurate so that simulations using this method were performed for a cutoff radii of $R_c = 20$, 40, and 60 Å. A good agreement was observed in the potential energies of the simulations with the DC method with R_c of 40 and 60 Å, suggesting that the DC method with $R_c = 40$ Å represents a converged result, as shown in Figs. 8(a)–9(b). Two other simulations were performed with the coupled DC + PPPM method with a cutoff radii of $R_c =$ 12 and 20 Å, respectively. It can be seen in the figures that the results are generally more sensitive to the cutoff radius for the DC+PPPM than the DC method.

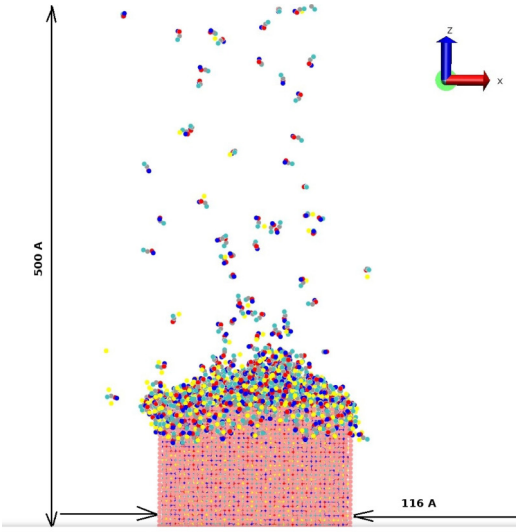

(a)

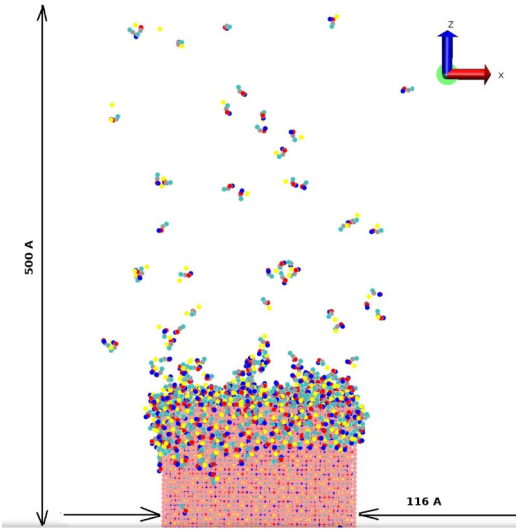

(b)

FIG. 7. Emission snapshot for the DC (a) and coupled DC + PPPM (b) method. The copper colored particles are the platinum sites that form the capillary, the light blue colored particles represent the M1 CG site, silver colored represent the IM CG site, red colored particles represent the MR CG site, dark blue colored particles represent the M2 CG site, and yellow colored particles represent the anion of BF4 CG sites.

The potential and kinetic energies for all ions, i.e., inside and outside the capillary, are shown in Figs. 8(a) and 8(b), respectively. Since the changes in the covalent and van der Waal's interactions are insignificant in the presence of an external electric field compared to the changes in the Coulomb energy, the Coulomb energy is considered representative of the total potential energy of the system. The kinetic energy as a function of time for the two methods are seen to be significantly different in Fig. 8(a) even after increasing the cutoff radius for the coupled DC + PPPM method. The system with lower potential energy (less negative) will have more emissions and therefore, higher kinetic energy. The highest Coulombic energy (most negative) was observed when only the

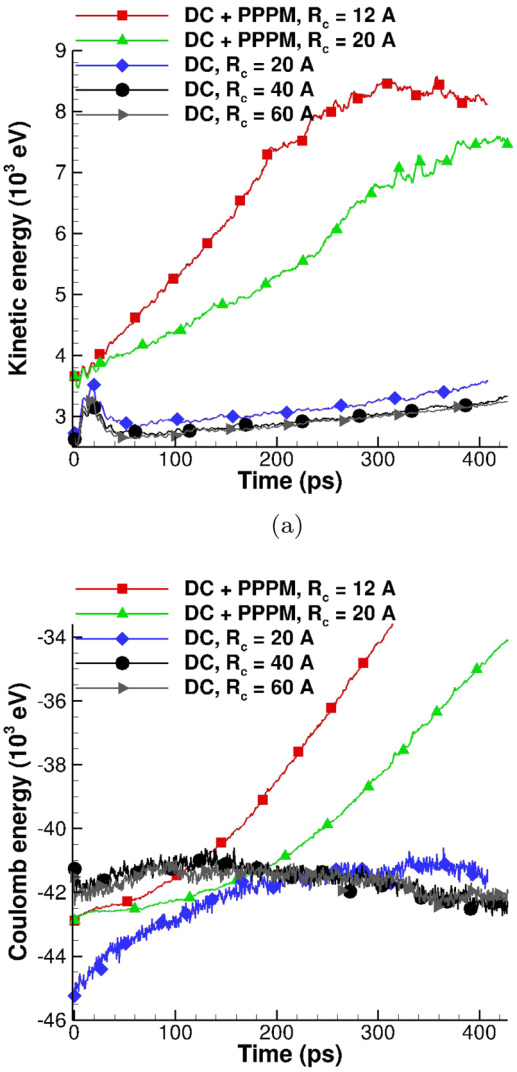

FIG. 8. Comparison of kinetic (a) and Coulombic energy (short+long range) (b) for the direct Coulomb (DC) with $R_c = 20$ Å and $R_c = 40$ Å, and DC + PPPM method with $R_c = 12$ Å and 20 Å.

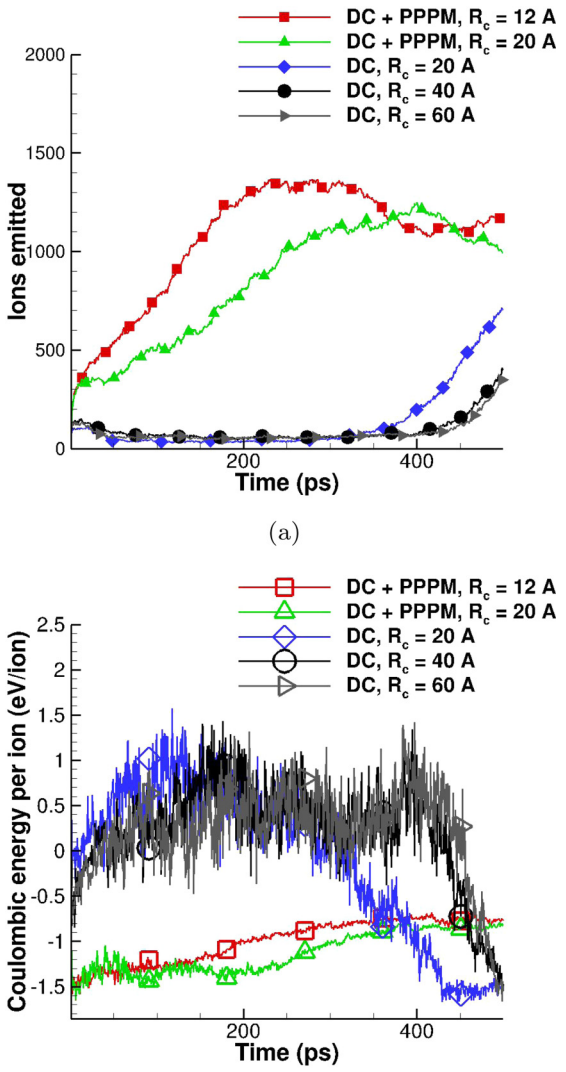

FIG. 9. Comparison of number of ions emitted (a) and Coulombic energy per ion of emitted ions (b) for the direct Coulomb (DC) with $R_c = 20$ Å and $R_c = 40$ Å, and DC + PPPM method with $R_c = 12$ Å and 20 Å.

DC method was used. We observed that the potential energy of the system with the DC method and $R_c = 20$ Å implementation had a higher potential energy (more negative), representing stronger Coulomb energy interactions in the system than for the simulations with coupled DC + PPPM method. For the DC method with a large cutoff radius (>40 Å), the initial potential energy was found to be lower (less negative) than predicted by the other methods due to the loose ions present at the meniscus of the capillary. As these few initial ions were emitted, prior to 150 ps, the Coulomb energy of the DC methods was stronger compared to the coupled DC + PPPM approach. As the cutoff radius for the coupled DC + PPPM systems was increased, the Coulomb energy of the system became comparatively stronger (more negative). However, for the coupled DC + PPPM system, even after increasing the R_c to 20 Å from $R_c =$ 12 Å, the Coulomb energy did not match with that of the DC method for a $R_c = 20$ Å.

This lack of agreement between the DC and DC+PPPM can be understood, given the approach that MD packages such as LAMMPS use. The general algorithm for long-range Coulomb interaction modes is to ensure that the short-range Coulomb energy approximates the long-range Coulomb energy at the cutoff radius to provide smooth transitioning between the short- and long-range potentials. This leads to truncation of the Coulomb energy for the coupled DC + PPPM method even when the cutoff radius was increased to 20 Å. The combined effect of dampening the short-range interactions for the DC + PPPM coupled systems and the long-range interactions resulted in weaker (less negative) Coulombic energies compared to simulations with only the DC method.

The lower Coulomb energy (less negative) for the coupled DC + PPPM method facilitated the emission of ions from the capillary, leading to higher emission rates, as seen in Fig. 9(a). The combination of stronger Coulomb interactions

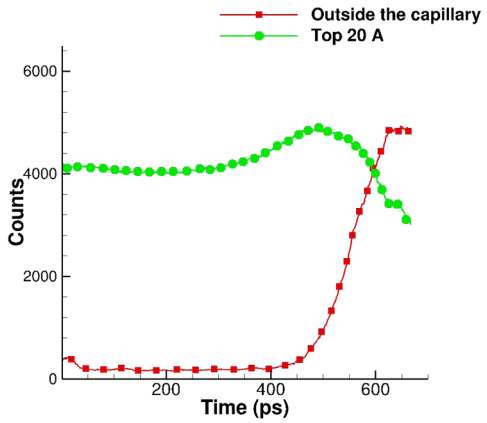

(a)

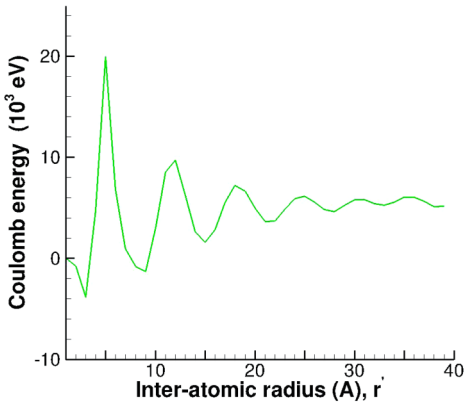

(b)

FIG. 10. Comparison of ion counts (a) and evaluation of Eq. (3) as a function of r' (b) for the direct Coulomb (DC) simulation at a mass flow rate of 1.22×10^{-12} kg/s. The green curve (circle symbols) in (a) shows the number of ions inside the capillary within $R_c = 20$ Å from the ions at the base of the Taylor cone ~1 Å above the meniscus.

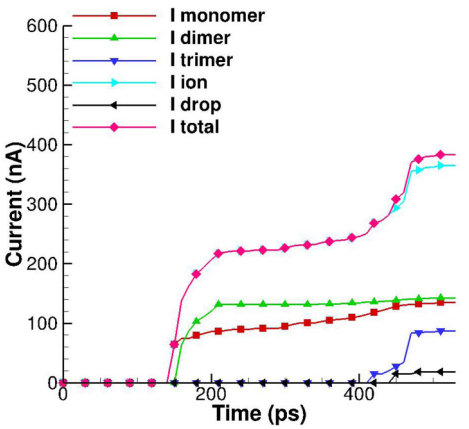

(a)

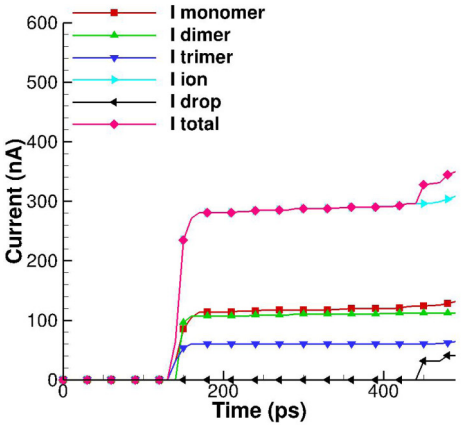

(b)

FIG. 11. Emission currents obtained for the direct Coulomb (DC) with $R_c = 20$ Å (a) and $R_c = 40$ Å (b).

enhanced the formation of a Taylor cone using the DC method as was shown in Fig. 7(a), as opposed to the disrupted structure observed for the DC + PPPM coupled method, shown in Fig. 7(b). The DC methods for both cutoff radii have similar emission trends and show minor differences only after 400-ps simulation time. Furthermore, when the Coulomb energy per ion of only the emitted ions was considered, the selection of cutoff radius for both the DC and the coupled DC + PPPM caused very little change, as shown in Fig. 9(b). The differences in the trends for these two methods is similar to that shown previously in Fig. 6(b).

The Coulomb interaction of the emitted ions and the ions present in the capillary just below the meniscus plays an important role in determining the statistics of ion emission even when only the pure DC method is used. Figure 10(a) shows the number or ions emitted from the capillary (outside the capillary) as a function of simulation time. The second curve labeled "Top 20 Å" identifies those ions inside the capillary that fall within a cutoff radius of 20 Å from the base of the Taylor cone. The interactions between these ions pairs strongly influence the Taylor cone structure. When this cutoff radius is increased to 40 Å, not surprisingly the number of ions present within the top 40 Å is twice that of ions present in the top 20 Å. Both the number of ions within the capillary and external to the capillary remain relatively constant until around 500 ps when the Taylor cone formation begins. To understand how the summation in Eq. (3) depends on the choice of R_c, the Coulomb energy was calculated for this system using the ion positions from an MD snapshot taken at 500 ps as a function of a sphere of influence, for $0 \leqslant r' \leqslant R_c$ for each ion in the domain. Figure 10(b) shows that for small r' values the Coulomb energy oscillates as additional ion pairs are added to the summation, however, at larger r' the magnitude of the oscillations decreases. Nevertheless, for even a conventional cutoff radius of $R_c = 12$ Å, fluctuations were observed in the measured Coulomb energy suggesting that a simulation performed with this value would not result in physically converged emission predictions. The figure shows that the amplitude of the fluctuations are essentially completely damped for a higher cutoff radius of $R_c = 40$ Å, although, this in general results in very high computational costs. Therefore, selecting a cutoff radius of at least 20 Å will provide a better assessment for ion electrospray simulations than the usual cutoff radius of $R_c = 12$ Å.

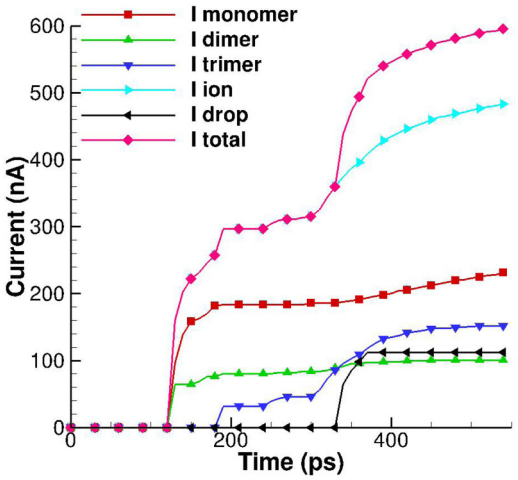

(a)

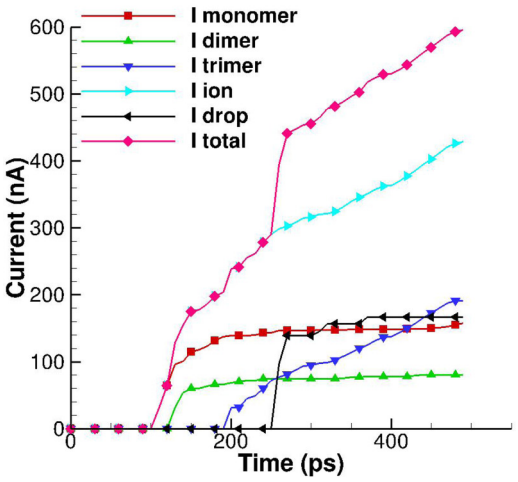

(b)

FIG. 12. Emission currents obtained for the DC + PPPM method with $R_c = 12$ Å (a) and 20 Å (b).

The effect of cutoff radii on the emission currents is shown in Figs. 11 and 12. The stronger (more negative) Coulomb interactions generated by the DC, $R_c = 20$ Å method cause slow but stable emission of ions, with monomers and dimers as the most dominant emitted species, as shown in Fig. 11(a). The ion emission trends for the DC cases shown in Fig. 9(a) are similar for increased cutoff radius from $R_c = 20$ to 40 Å. This explains why the emission currents presented in Fig. 11(b) are unchanged even for larger R_c values. Figure 12(a) shows that the weaker (less negative) Coulombic interactions for the coupled DC + PPPM simulations, especially for a lower cutoff radius, $R_c = 12$ Å, allowed for easier emission resulting in comparatively higher emission currents than the DC method. The ease of emission for the coupled DC + PPPM method also leads to emission of larger ion species from the capillary. Whereas the DC method predicted low emission currents of trimers and droplets, the coupled DC + PPPM method showed considerably higher trimer and droplet currents. Extending the cutoff radius for the coupled DC + PPPM from 12 to 20 Å caused the total currents to be marginally lower, but they were still significantly higher than the DC method, as shown in Fig. 12(b).

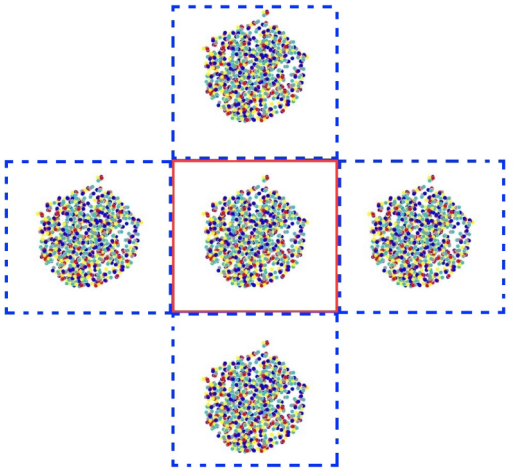

FIG. 13. Plan view (x-y plane) of the domain images (blue, dashed) created around the actual domain (red, solid) due to periodicity. Sides of the square represent 500 Å.

C. Effect of periodicity on the electrospray emissions

When MD simulations of bulk physical properties, such as mass density and electrical conductivity, are conducted for ionic liquids, one typically assumes that the system is periodic to reduce the number of required simulated atoms. But in case of the electrospray simulations, the IL liquid is contained within a capillary which is placed in its entirety in the simulation domain. This makes it necessary to question whether it is correct to implement periodicity in the electrospray MD simulations. In fact, the use of the PPPM method to model nonperiodic domains has been reported to generate incorrect results by Luty *et al.* [37]. For the results discussed in this paper, the simulation domain was considered periodic in the x-y direction and nonperiodic in the extrusion or the z direction. As shown in Fig. 13, periodicity in the x and y creates nonphysical images around the actual domain. These images are generated at the domain boundaries and also contribute to the Coulomb interaction calculations.

To analyze the effects of periodicity, MD simulations were performed for both the DC and the coupled DC + PPPM methods by modifying the domain constraints to make all three dimensions nonperiodic. However, the coupled DC + PPPM could not be performed on a nonperiodic domain in MD and so to approximate a nonperiodic domain, the size of the domain shown in Fig. 2(a) was increased in the x and y directions to 2000 Å. Accordingly, the periodic images generated were far enough from the actual simulated domain that their influence on the energy of the system was negligible. This allowed us to calculate the potential, kinetic, and Coulomb energy without the contributions from the nonphysical images for the coupled DC + PPPM method.

The Coulomb energy comparison of the periodic and nonperiodic DC and coupled DC + PPPM methods is shown in Fig. 14(a). Changing the periodicity did not affect the simulation performed using the DC method but changed the emission

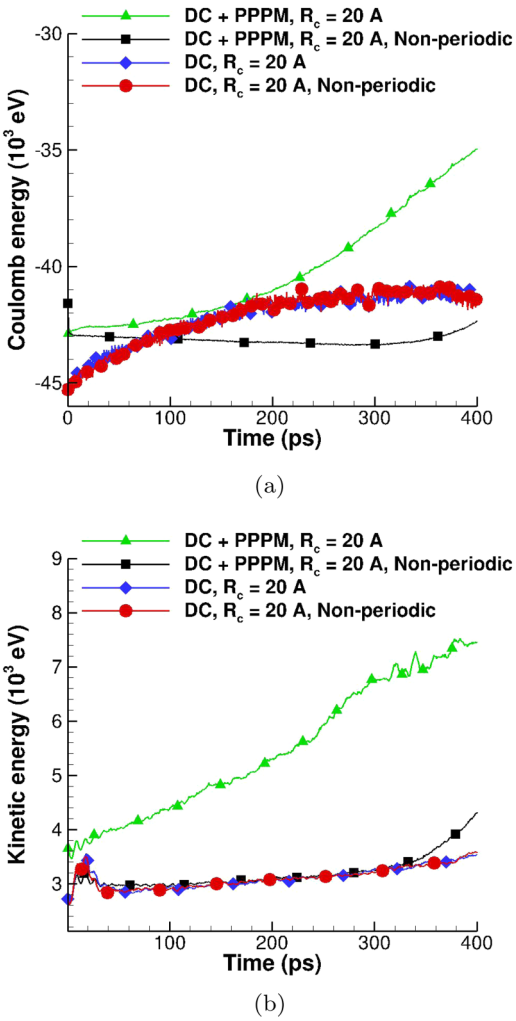

FIG. 14. Comparison of Coulombic energy (short+long range) (a) and kinetic energy (b) for the nonperiodic direct Coulomb (DC) with $R_c = 20$ Å and nonperiodic DC + PPPM method with $R_c = 20$ Å.

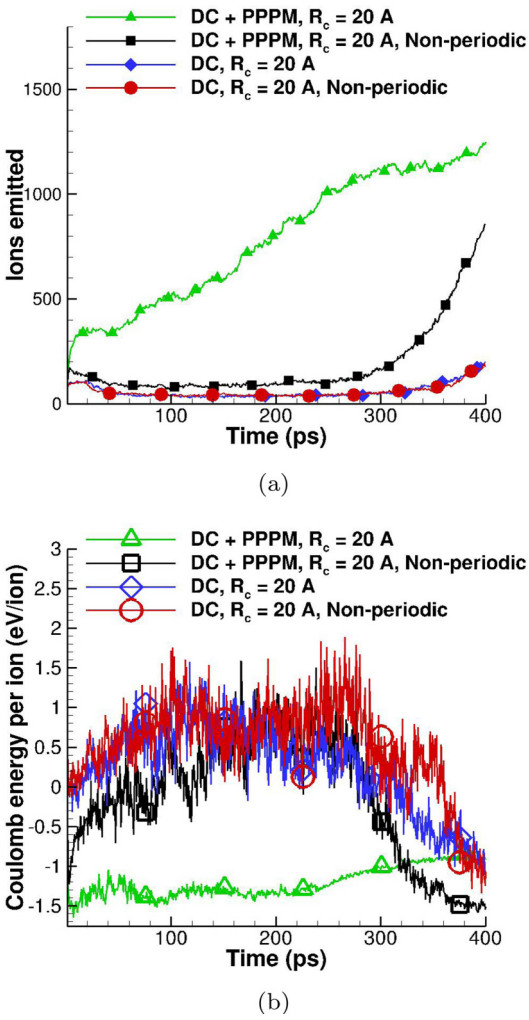

FIG. 15. Comparison of number of ions emitted (a) and Coulombic energy per ion of ions emitted (b) for the nonperiodic direct Coulomb (DC) with $R_c = 20$ Å and nonperiodic DC + PPPM method with $R_c = 20$ Å.

behavior for the coupled DC + PPPM method. The potential energy for the nonperiodic coupled DC + PPPM method was closer in trend to the DC method rather than the periodic coupled DC + PPPM results. The kinetic energy of the periodic DC, nonperiodic DC, and nonperiodic coupled DC + PPPM cases showed remarkable agreement in Fig. 14(b), suggesting similar emission characteristics. The ion emission rate and the Coulomb energy per ion of the emitted ions for the nonperiodic coupled DC + PPPM method are in closer agreement with the results obtained by the DC method, as shown in Figs. 15(a) and 15(b), respectively. The assumption of periodicity does produce important changes in the emission behavior and should not be implemented for the electrospray simulations performed for the configuration shown in Fig. 2(b). Increasing the domain size of the coupled DC + PPPM simulations to make it nonperiodic increases the computational cost and makes it computationally twice as expensive than the nonperiodic DC method with $R_c = 20$ Å. Therefore, in contrast to the general perception, the DC method gives the best physical results for these types of MD simulations at the lowest possible computational cost. However, it should be noted that the DC method with $R_c = 40$ Å is five times more expensive than the simulations with nonperiodic DC method and $R_c = 20$ Å.

V. CONCLUSION

The choice of the long-range Coulombic interaction model dictates the emission behavior observed from the MD simulation. Comparison of the DC+PPPM and SFCS methods with the exact DC approach showed that the SFCS underpredicts the Coulomb interactions thereby generating very high emission currents. The DC+PPPM method, while efficient, was not able to reproduce the Coulomb energy trends obtained by the exact DC method. For both the DC and DC+PPPM methods, the Coulomb interaction cutoff radius has an effect on the emission currents, kinetic and Coulomb energies, Coulomb energy per emitted ion, and number of ions emitted. The DC+PPPM results appear to be more sensitive to this parameter than the DC approach. With respect to the DC approach, convergence in the above mentioned physical parameters is achieved for

$R_c = 40$ Å, however, the relative difference in the Coulomb energies for emitted ions and currents between $R_c = 20$ and 40 Å does not warrant the five times higher computational cost necessary to perform simulations with a cutoff radius of 40 Å. Although, useful for accurate simulations of bulk IL physical properties, domain periodicity incorrectly alters the emission characteristics for the coupled DC + PPPM method for the extrusion geometries modeled in this work. For this reason, it is recommended that to model the strong Coulomb interactions in ILs with the highest fidelity, a nonperiodic domain using the DC method and a value of $R_c = 20$ Å be used in MD electrospray simulations.

It should be noted that generating emission and Taylor cone structure during the MD electrospray simulations is not only dependent on the long-range Coulomb models, cutoff radius, and periodicity but also on the external electric field boundary conditions. The radial components of the electric field creates lateral movement of ion pairs at the mouth of the capillary, causing the meniscus to deform into a Taylor cone structure. Further work is necessary to access accurate electric boundary conditions relevant to electrospray MD simulations.

ACKNOWLEDGMENTS

Funding for this work was provided by the Air Force Office of Scientific Research (AFOSR) through Dr. Mittat Birkan under Grant No. AF FA9550-16-1-0193. We are thankful to the Department of Defense for providing us with the vital computational resources on their GARNET and to XSEDE TACC for their use of the STAMPEDE2 cluster.

[1] G. I. Taylor, Disintegration of water droplets in an electric field, Proc. R. Soc. London A **280**, 383 (1964).
[2] W. Deng, C. Mike Waits, and A. Gomez, Digital electrospray for controlled deposition, Rev. Sci. Instrum. **81**, 035114 (2010).
[3] A. Jaworek, Electrospray droplet sources for thin film deposition, J. Mater. Sci. **42**, 266 (2007).
[4] L. W. Swanson, Liquid metal ion sources: Mechanism and applications, Nucl. Instrum. Methods Phys. Res. **218**, 347 (1983).
[5] R. Clampitt, Advances in molten metal field ion sources, Nucl. Instrum. Methods Phys. Res. **189**, 111 (1981).
[6] Y. Wu, S. J. Kennedy, and R. L. Clark, Polymeric particle formation through electrospraying at low atmospheric pressure, J. Biomed. Mater. Res. B **90B**, 381 (2009).
[7] W. Zhu, N. J. Castro, X. Cheng, M. Keidar, and L. G. Zhang, Cold atmospheric plasma modified electrospun scaffolds with embedded microspheres for improved cartilage regeneration, PLoS One **10**, e0134729 (2015).
[8] B. Wu and J. S. Becker, Imaging of elements and molecules in biological tissues and cells in the low-micrometer and nanometer range, Int. J. Mass Spectrom. **307**, 112 (2011).
[9] S. N. Jayasinghe and A. C. Sullivan, Electrospraying: an *in-situ* polymerisation route for fabricating high macroporous scaffolds, J. Sol-Gel Sci. Technol. **38**, 293 (2006).
[10] S. N. Jayasinghe, A. N. Qureshi, and P. A. M. Eagles, Electrohydrodynamic jet processing: An advanced electric-field-driven jetting phenomenon for processing living cells, Small **2**, 216 (2006).
[11] R. Toniolo, A. Pizzariello, N. Dossi, S. Lorenzon, O. Abollino, and G. Bontempelli, Room temperature ionic liquids as useful overlayers for estimating food quality from their odor analysis by quartz crystal microbalance measurements, Anal. Chem. **85**, 7241 (2013).
[12] J. M Deitzel, J. Kleinmeyer, D. Harris, and N. C. B. Tan, The effect of processing variables on the morphology of electrospun nanofibers and textiles, Polymer **42**, 261 (2001).
[13] J. Jirsak, F. Moucka, and I. Nezbeda, Insight into electrospinning via molecular simulations, Ind. Eng. Chem. Res. **53**, 8257 (2014).
[14] J. B. Fenn, M. Mann, C. K. Meng, S. F. Wong, and C. M. Whitehouse, Electrospray ionization for mass spectrometry of large biomolecules, Science **246**, 64 (1989).
[15] B. Donius and J. L. Rovey, Ionic liquid dual-mode spacecraft propulsion assessment, J. Spacecr. Rockets **48**, 110 (2011).
[16] B. D. Prince, P. Tiruppathi, R. J. Bemish, Yu-Hui Chiu, and E. J. Maginn, Molecular dynamics simulations of 1-ethyl-3-methylimidazolium bis[(trifluoromethyl)sulfonyl]imide clusters and nanodrops, J. Phys. Chem. A **119**, 352 (2015).
[17] W. L. Jorgensen, D. S. Maxwell, and J. Tirado-Rives, Development and testing of the OPLS all-atom force field on conformational energetics and properties of organic liquids, J. Am. Chem. Soc. **118**, 11225 (1996).
[18] D. Y. Kim and M. M. Micci, Molecular dynamics simulations of a liquid gallium electrospray thruster, J. Propul. Power **29**, 899 (2013).
[19] A. Borner and D. A. Levin, Use of advanced particle methods in modeling space propulsion and its supersonic expansions, Ph.D thesis, Penn State University, 2014.
[20] H. Weingartner, Understanding ionic liquids at the molecular level: Facts, problems, and controversies, Angew. Chem. Int. Ed. **47**, 654 (2008).
[21] B. S. Lee and S. T. Lin, The role of long-range interactions in the phase behavior of ionic liquids, PCCP **14**, 6520 (2012).
[22] C. L. Brooks, B. Montgomery Pettitt, and M. Kerplus, Structural and energetic effects of truncating long ranges interactions in ionic and polar fluids, J. Chem. Phys. **83**, 5897 (1985).
[23] S. Plimpton, Fast parallel algorithms for short-range molecular dynamics, J. Comput. Phys. **117**, 1 (1995).
[24] Y. Wang, W. G. Noid, and G. A. Voth, Effective field coarse graining, PCCP **11**, 2002 (2009).
[25] Y. Wang, S. Izvekov, T. Yan, and G. A. Voth, Multiscale coarse-graining of ionic liquids, J. Phys. Chem. B **110**, 3564 (2005).
[26] See Supplemental Material at http://link.aps.org/supplemental/10.1103/PhysRevE.97.033306 for the bonded and nonbonded CG potentials used for this work.
[27] J. V. L. Beckers, C. P. Lowe, and S. W. De Leeuw, An iterative PPPM method for simulating Coulombic systems on distributed memory parallel computers, Mol. Simul. **20**, 369 (1998).
[28] C. J. Fennell and J. D. Gezelter, Is the Ewald summation still necessary? Pairwise alternatives to the accepted standard for long-range electrostatics, J. Chem. Phys. **124**, 234104 (2006).

[29] R. W. Hockney and J. W. Eastwood, *Computer Simulations Using Particles* (CRC Press Taylor and Francis Group, Philadelphia, 1988).

[30] E.L. Pollock and J. Glosli, Comments on P3M, FMM, and the Ewald method for large periodic Coulombic systems, Comput. Phys. Commun. **95**, 93 (1996).

[31] T. Darden, D. York, and L. Pedersen, Particle mesh Ewald: An N·log(N) method for Ewald sums in large systems, J. Chem. Phys. **98**, 10089 (1993).

[32] A. Y. Toukmaji and J. A. Board, Ewald summation techniques in perspective: a survey, Comput. Phys. Commun. **95**, 73 (1996).

[33] Y. Saad and M. H. Schultz, Gmres: A generalized minimal residual algorithm for solving nonsymmetric linear systems, SIAM J. Sci. Comput. **7**, 856 (1986).

[34] A. Borner and D. Levin, Coupled molecular dynamics - three-dimensional Poisson simulations of ionic liquid electrospray thrusters, IEEE Trans. Plasma Sci. **34**, 1 (2015).

[35] A. Borner, P. Wang, and D. A. Levin, Influence of electrical boundary conditions on molecular dynamics simulations of ionic liquid electrosprays, Phys. Rev. E **90**, 063303 (2014).

[36] I. Romero-Sanz, R. Bocanegra, J. Fernandez de la Mora, and M. Gamero-Castano, Source of heavy molecular ions based on Taylor cones of ionic liquids operating in the pure ion evaporation regime, J. Appl. Phys. **94**, 3599 (2003).

[37] Brock A. Luty and Wilfred F. van Gunsteren, Calculating electrostatic interactions using the particle–particle particle–mesh method with nonperiodic long-range interactions, J. Phys. Chem. **100**, 2581 (1996).